

# Electrical and impedance spectroscopy analysis of sol-gel derived spin coated $\text{Cu}_2\text{ZnSnS}_4$ solar cell

Goutam Kumar Gupta, Ashish Garg, and Ambesh Dixit

Citation: *Journal of Applied Physics* **123**, 013101 (2018);

View online: <https://doi.org/10.1063/1.5002619>

View Table of Contents: <http://aip.scitation.org/toc/jap/123/1>

Published by the *American Institute of Physics*

---

## Articles you may be interested in

[Three-dimensional hybrid silicon nanostructures for surface enhanced Raman spectroscopy based molecular detection](#)

*Journal of Applied Physics* **123**, 014301 (2018); 10.1063/1.5000994

[Edge enhanced growth induced shape transition in the formation of GaN nanowall network](#)

*Journal of Applied Physics* **123**, 014302 (2018); 10.1063/1.5004496

[Self-assembly 2D zinc-phthalocyanine heterojunction: An ideal platform for high efficiency solar cell](#)

*Applied Physics Letters* **111**, 253904 (2017); 10.1063/1.5005119

[Burying non-radiative defects in InGaN underlayer to increase InGaN/GaN quantum well efficiency](#)

*Applied Physics Letters* **111**, 262101 (2017); 10.1063/1.5007616

[Modulating PL and electronic structures of  \$\text{MoS}\_2\$ /graphene heterostructures via interlayer twisting angle](#)

*Applied Physics Letters* **111**, 263106 (2017); 10.1063/1.5011120

[Effect of Cd doping on magnetocaloric effect and critical behavior analysis on perovskite  \$\text{Nd}\_{1-x}\text{Cd}\_x\text{MnO}\_3\$  \( \$x = 0, 0.1, 0.2, 0.3, \text{ and } 0.4\$ \) manganite polycrystals](#)

*Journal of Applied Physics* **122**, 245109 (2017); 10.1063/1.5010427

---

**Scilight**

Sharp, quick summaries **illuminating**  
the latest physics research

Sign up for **FREE!**



# Electrical and impedance spectroscopy analysis of sol-gel derived spin coated $\text{Cu}_2\text{ZnSnS}_4$ solar cell

Goutam Kumar Gupta,<sup>1</sup> Ashish Garg,<sup>2</sup> and Ambesh Dixit<sup>1,a)</sup>

<sup>1</sup>Department of Physics and Center for Solar Energy, Indian Institute of Technology Jodhpur, Rajasthan 342011, India

<sup>2</sup>Department of Materials Science and Engineering, Indian Institute of Technology Kanpur, Kanpur 208016, India

(Received 31 August 2017; accepted 11 December 2017; published online 3 January 2018)

We carried out electrical and impedance studies on solution derived Al:ZnO/ZnO/CdS/ $\text{Cu}_2\text{ZnSnS}_4$ /Mo/Glass multilayered solar cell structures to understand their impact on photovoltaic performance. The  $\text{Cu}_2\text{ZnSnS}_4$  layer is synthesized on a molybdenum (Mo) coated soda lime glass substrate as an absorber and characterized intensively to optimize the absorber physical properties. The optimized  $\text{Cu}_2\text{ZnSnS}_4$  is p-type with  $5.8 \times 10^{17} \text{ cm}^{-3}$  hole carrier concentration. The depletion width of the junction is around 20.5 nm and the diffusion capacitance is  $\sim 35.5 \text{ nF}$  for these devices. We observed relatively large minority carrier life time  $\sim 23 \mu\text{s}$  for these structures using open voltage decay analysis. The measured  $\text{Cu}_2\text{ZnSnS}_4/\text{MoS}_2$  and  $\text{Cu}_2\text{ZnSnS}_4/\text{CdS}$  interface resistances are  $7.6 \text{ k}\Omega$  and  $12.5 \text{ k}\Omega$ , respectively. The spatial inhomogeneities are considered and the corresponding resistance is  $\sim 11.4 \text{ k}\Omega$ . The impedance measurements suggest that in conjunction with series resistance  $\sim 350 \Omega$ , the interface and spatial inhomogeneity resistances also give a significant contribution to the photovoltaic performance. *Published by AIP Publishing.*

<https://doi.org/10.1063/1.5002619>

## I. INTRODUCTION

Silicon based solar photovoltaic devices are already in widespread use for energy generation, including the small scale distributed applications to the large scale power plants.<sup>1</sup> While the cost of poly-silicon based technologies has come down tremendously over the last few years, their efficiencies remain low and as a result, the area coverage is very high. Considerable progress has been made and numerous alternative materials have been demonstrated over years such as copper indium gallium selenide (CIGS),<sup>2</sup> cadmium telluride (CdTe),<sup>3</sup> solid state, and dye/quantum dot sensitized liquid electrolyte based solar cells<sup>4</sup> as well as polymer solar cells.<sup>5,6</sup> Among these, inorganic thin film based CIGS and CdTe are considered favourable because of their considerably high power conversion efficiencies along with excellent environmental stability. However, toxicity of constituent elements, namely, Cd, Ga, and Se and natural scarcity of indium pose concerns on their long term sustainability and related environmental issues for CIGS and CdTe based solar photovoltaic systems.

A cheaper and relatively less toxic alternative to CIGS is copper zinc tin sulfide (CZTS) with abundantly available elements and is considered as a promising replacement of CIGS based solar absorber materials for thin film heterostructure based solar photovoltaic devices. The material possesses an optimum direct band gap of  $E_g \sim 1.5 \text{ eV}$  and exhibit a high absorption coefficient ( $>10^4 \text{ cm}^{-1}$ ) making it extremely appropriate for photovoltaic applications. There are continuous efforts to harness the potential of CZTS absorber materials for energy conversion and CZTS based

solar cell devices have achieved efficiency exceeding 12% after alloying with selenium<sup>7,8</sup> with a maximum efficiency of  $\sim 12.7\%$  reported for CZTS,Se solar cells with double  $\text{In}_2\text{S}_3/\text{CdS}$  buffer layer emitter structures.<sup>9</sup> However, in general, CZTS solar cells with kesterite phase suffer from lower device efficiencies. The main reason for relatively lower efficiency of kesterite phased photovoltaic devices is the high series resistance and poor open circuit voltage ( $V_{oc}$ ) as compared to their counterparts such as CIGS and CdTe based photovoltaic devices. The intrinsic high resistivity of CZTS in conjunction with the ease of Schottky contact formation with molybdenum (Mo) back contact offers high series resistance to the cell, leading to lower open circuit voltage.<sup>10</sup> The relatively lower defect activation energies as compared to that of the CZTS band gap and high recombination are also responsible for the observed lower open circuit voltage.<sup>11</sup> The antisite  $\text{Cu}_{\text{Zn}}$  deep acceptors and  $\text{Zn}_{\text{Cu}}$  donor states also cause the large potential fluctuation in CZTS photovoltaic systems.<sup>12</sup> These defect states may result in enhanced recombination at the CdS buffer layer and CZTS absorber layer heterojunction interface. This is contrary to the requirement of the minimum recombination loss in the space charge region near the hetero-interface, which is essential to realize the enhanced photovoltaic performance. These defect levels should be avoided or minimized at least. These can be avoided by ensuring the phase pure CZTS materials, where the antisite donor or acceptor defect levels are not observed in the band gap region. The vulnerability for the formation of secondary phases and defects in the CZTS material system make it very difficult to synthesize and thus, hamper the high efficiencies of CZTS kesterite photovoltaic systems. The vacuum processed CZTS-Se photovoltaic devices have

<sup>a)</sup>ambesh@iitj.ac.in

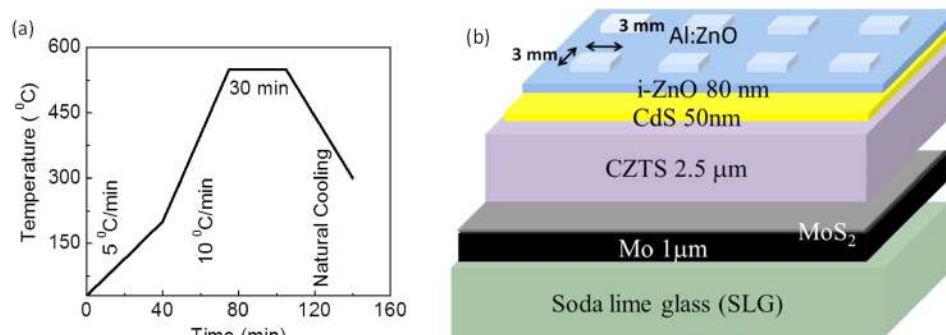


FIG. 1. (a) The temperature versus time profile with respective heating rates, used for post annealing of spin-coated CZTS/SLG and CZTS/Mo/SLG thin films under diluted H<sub>2</sub>S environmental conditions and (b) schematic multilayer Al:ZnO/ZnO/CdS/CZTS/Mo/SLG heterostructure solar cell structure, with top cuts, representing 3 mm × 3 mm individual solar cell structures.

shown the highest efficiency of  $\sim 9.15\%$  using evaporation and  $8.4\%$  using the sputtering process.<sup>13</sup> However, relatively low throughput, less material utilization, and costly fabrication processes make the vacuum assisted techniques difficult for large scale production. In contrast, non-vacuum techniques, such as sol-gel, electrodeposition, and nano particle based processes, are relatively less costly. However, such processes suffer from residual organic impurities and toxic additives used during the synthesis. Among these non-vacuum techniques, the sol-gel technique is relatively simpler and inexpensive. The process provides easy control on extrinsic doping such as alkali metals (Li, Na, K) and alloying with different materials such as Cd, Ge, etc. Thus, physical properties, such as carrier concentration, mobility, and bandgap, can be tailored to realize the enhanced photovoltaic response.<sup>14</sup> Several reports with significant efficiency showed potential for the sol-gel based spin coating technique for high throughput and high efficiency photovoltaic devices.<sup>15</sup> However, there are challenges in achieving enhanced efficiencies and the reported laboratory efficiencies showed a large variation from very low 0.1 to high 12% photovoltaic efficiencies for CZTS-Se solar cells and average efficiencies lie  $\sim 1\%$ – $2\%$  in general.<sup>16–25</sup> The large variation in photovoltaic efficiencies and the factors limiting the efficiencies can be understood by the detailed electrical and impedance characterization of these CZTS solution processed devices.

The present work details the fabrication of solution processed spin-coated CZTS thin film based Al:ZnO/ZnO/CdS/CZTS/Mo/Glass heterostructure solar cells. This work discusses the structural, morphological, and electrical properties of the absorber layer and fabricated solar cells. The open circuit voltage decay (OCVD) and impedance spectroscopy analysis have been performed at different bias potentials ranging from reverse bias to forward bias voltages under dark conditions. The measurements are used to understand the device parameters and their impact on device performance.

## II. EXPERIMENTAL DETAILS

### A. CZTS absorber material and Al:ZnO/ZnO/CdS/CZTS/Mo/Glass solar cell fabrication

The detailed synthesis process for the CZTS absorber layer has been reported elsewhere.<sup>26</sup> In brief, copper (II) chloride dehydrate, anhydrous zinc chloride, tin (II) chloride, and thiourea precursors are used for respective constituent Cu, Zn, Sn, and S elements in 2: 1.2: 1: 8 atomic ratio. These are

dissolved in 2-methoxyethanol for a very stable (over several months) sol. The excess atomic zinc concentration has intentionally been considered during the synthesis to achieve the zinc rich CZTS absorber layer, required for an enhanced photovoltaic response.<sup>27</sup> The stable sol has been used for spin coating to prepare CZTS thin films on soda lime glass (SLG) and molybdenum coated SLG substrates at 3500 rounds per minute (rpm) spinning speed. The spin coated layer has been backed at  $300^\circ\text{C}$  on a hot plate for 5 min, followed by cooling to room temperature. This process has been repeated several times to achieve the desired thickness. The prepared CZTS absorber thin film has been post annealed in a tubular furnace under a sulfur environment, maintained by the continuous flow of 5% H<sub>2</sub>S in argon during the heat treatment process. The temperature profile against time is shown in Fig. 1(a), used for annealing of CZTS thin films. A slower heating rate ( $5^\circ\text{C}/\text{min}$ ) has been opted up to  $200^\circ\text{C}$  to allow the proper alloying of constituent elements, following by fast heating at rate  $10^\circ\text{C}/\text{min}$  to  $550^\circ\text{C}$  for half an hour to minimize the loss of volatile tin during CZTS kesterite phase formation. The optimized CZTS absorber layer has been grown on 1 in. × 1 in. Mo coated ( $\sim 1.5\ \mu\text{m}$  thick) soda lime glass (SLG) substrate. The CdS buffer layer ( $\sim 50 \pm 20\ \text{nm}$ ) has been deposited on the CZTS absorber layer using a chemical bath. An intrinsic  $\sim 80 \pm 20\ \text{nm}$  ZnO layer has been deposited using RF sputtering, followed by conducting  $\sim 1\ \mu\text{m}$  Al:ZnO layer using the DC sputtering process. The schematic of the Al:ZnO/ZnO/CdS/CZTS/Mo/SLG heterostructure photovoltaic device is shown in Fig. 1(b), where the approximate thickness for each layer is also mentioned. The fabricated 1 in. × 1 in. structure has been divided into 3 mm × 3 mm solar cell structures, as shown in Fig. 1(b), to avoid the necessity of top metallic grids for efficient current collection.

### B. Characterization

The phase identification and structural information of CZTS absorber layers are investigated using a Bruker D8 Advance X-ray diffractometer, with a Cu K $\alpha$  ( $\lambda = 1.5406\ \text{\AA}$ ) monochromatic incident radiation source, operating at 40 kV and 40 mA current. The data were collected in locked couple mode with  $2\theta$  diffraction angle ranging from  $10^\circ$  to  $80^\circ$  at a  $0.02^\circ$  step size. Scanning electron microscopy (SEM) has been used to understand the morphological features with the surface microstructures in conjunction with energy dispersive X-ray (EDX) spectroscopy measurements for elemental compositions, using EVO 18, special edition, Carl Zeiss

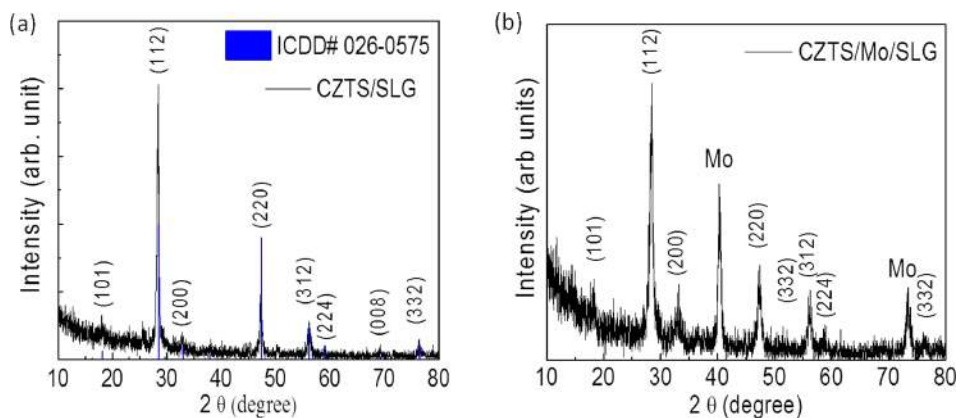


FIG. 2. X-ray diffraction pattern of the post annealed CZTS thin films on (a) SLG substrate (CZTS/SLG), with the reference kesterite CZTS phase (ICDD# 026-0575) and (b) Mo/SLG substrate (CZTS/Mo/SLG).

scanning electron microscope (SEM) (oxford instrument make) attached as an energy dispersive X-ray detector. The diffuse reflectance was measured using a Cary 4000 UV-Vis spectrophotometer in the 200 nm to 900 nm spectral range. The polytetrafluoroethylene (PTFE) sample was used as a reference for the diffuse reflectance measurements. The electrical responses such as open circuit voltage decay (OCVD), impedance measurements, and the photoactive current–voltage analysis are performed using an Autolab PGSTAT302N (Matrohm make) electrochemical workstation equipped with a frequency analyzer unit for the fabricated solar photovoltaic devices. These measurements are performed in the dark and one sun illumination ( $1000 \text{ W/m}^2$ ) conditions. The impedance measurements are carried out using a 10 mV AC perturbation in the 1 Hz to 1 MHz frequency range. The capacitance-voltage (C-V) measurements are carried out for fabricated photovoltaic devices for the  $-1 \text{ V}$  to  $1 \text{ V}$  potential range at different frequencies.

### III. RESULTS AND DISCUSSION

#### A. Structural and microstructural characterization

The X-ray diffraction (XRD) pattern is shown in Fig. 2 for the prepared CZTS absorber thin film on the SLG substrate Fig. 2(a) and Mo coated SLG substrate Fig. 2(b). The standard kesterite phase diffraction data (ICDD PDF # 260575) are also plotted in Fig. 2(a), with relative intensity for the respective diffraction peaks. The measured XRD peaks are consistent with the reference, where all the diffraction peaks are indexed completely, suggesting the formation of a CZTS kesterite crystallographic phase.

The four main diffractions peaks are observed at about  $28.46^\circ$ ,  $47.32^\circ$ ,  $56.22^\circ$ , and  $76.48^\circ$  corresponding to (112), (220), (312), and (332) diffraction planes for the kesterite

CZTS phase. CZTS thin films, thus formed, are polycrystalline in nature with relatively enhanced texturing along the (112) direction. The grain size was measured using the Scherrer equation  $D = \frac{K\lambda}{\beta \cos \theta}$ , where  $K = 0.94$ ,  $\lambda$  is wavelength of characteristic Cu K $\alpha$  X-ray incident radiation,  $\beta$  is the full width half maxima (FWHM) of the diffraction peaks in radian, and  $\theta$  is the respective diffraction position.<sup>28</sup> The measured crystallite size is  $\sim 24.37 \text{ nm}$  for the synthesized CZTS absorber layers. The Williamson and Smallman equation  $\delta = 1/D^2$ , where  $D$  is the average crystallite size, suggests the large dislocation density  $\sim 1.683 \times 10^{15} \text{ lines m}^{-2}$  in these CZTS thin films.<sup>29</sup> The lattice strain ‘ $\epsilon$ ’ has been measured using  $\epsilon = \beta_{hkl}/4 \tan \theta$ , where  $\beta_{hkl}$  is full width half maxima for the (hkl) diffraction plane and  $\theta$  is the respective diffraction position and values are summarized in Table I.<sup>30</sup> The strain values are of the order of  $\sim 10^{-3}$ , suggesting negligible strain which is because of the large thickness of CZTS thin films. The representative X-ray diffraction pattern of CZTS thin films, coated on Mo/SLG substrates and used for solar cell fabrication, is shown in Fig. 2(b). The measurements suggest that crystallographic texture along  $\langle 112 \rangle$  has improved without any impurity, including the MoS<sub>2</sub> interfacial layer at the CZTS/Mo interface within the XRD detection limits. Furthermore, Raman spectroscopy measurements on identical films reported elsewhere<sup>26</sup> also substantiate the phase purity of the synthesized CZTS absorber layer in conjunction with XRD measurements.

The microstructural analysis and measurement of elemental composition of the CZTS absorber thin film are carried out using scanning electron microscopy (SEM) and energy dispersive x-ray (EDX) measurements. The surface SEM micrograph is shown in Fig. 3(a). The uniform and smooth granular growth can be observed over the entire surface of the CZTS thin film [Fig. 3(a)]. The elemental

TABLE I. The crystallographic and thin film parameters, derived from the X-ray diffraction measurements (Fig. 2).

Samples	$\langle hkl \rangle$	$2\theta$ (deg) (observed)	FWHM (deg)	$d_{\text{exp}}$ (Å)	Strain $\epsilon$ ( $\times 10^{-3}$ )	Grain size D (nm)	Average grain size (nm)	Dislocation density $\delta$ (lines $\text{m}^{-2}$ )	Lattice parameter (a = b, and c), measured (Å)
CZTS	(112)	28.46	0.385	3.133	6.62	22.23	$24.37 \pm 6$	$1.683 \pm 0.0006 \times 10^{15}$	A = b = 5.427 c = 10.848 c/2a = 0.9994
	(220)	47.32	0.395	1.919	3.93	22.93			
	(312)	56.22	0.428	1.635	3.49	21.97			
	(332)	76.48	0.348	1.244	1.92	30.35			

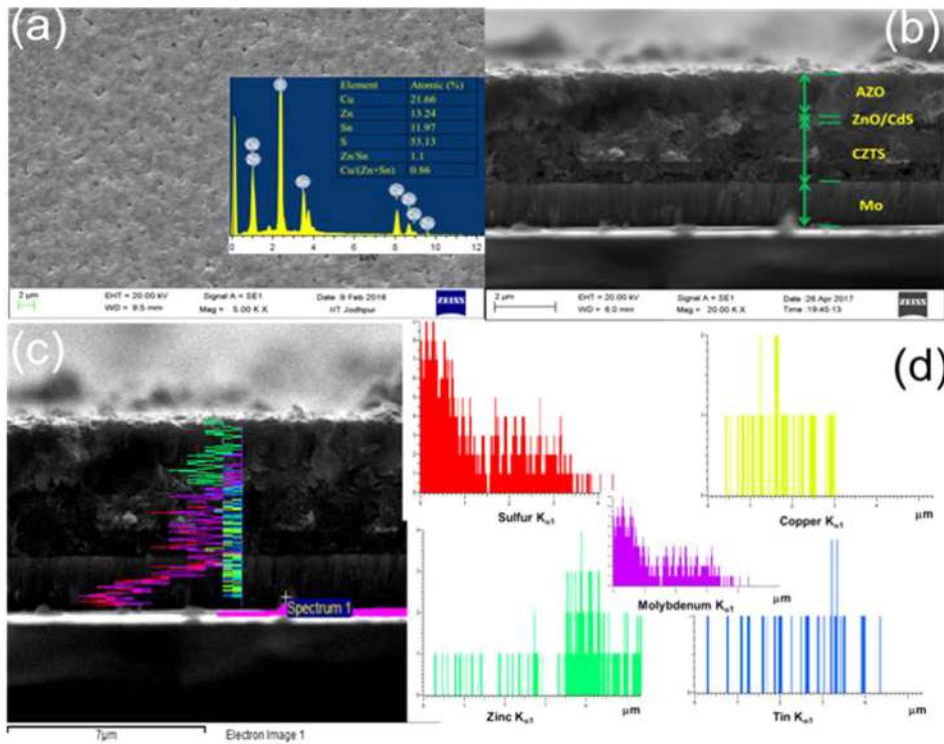


FIG. 3. Scanning electron micrograph (a) of the CZTS absorber thin film over the Mo coated SLG substrate (inset showing elemental composition obtained through EDAX spectroscopy); (b) cross sectional view of stacked layers for the AZO/ZnO/CdS/CZTS/Mo/SLG heterostructure solar cell; (c) summed elemental mapping across the Mo/CZTS interface; and (d) respective elemental distribution across the interface.

compositional analysis shown in the inset of Fig. 3(a) suggests that grown CZTS thin films are copper deficient and zinc rich in composition.

These results are consistent with the growth conditions, where the excess Zn precursor has been used to achieve the observed configuration.<sup>31</sup> The cross-sectional micrograph is shown in Fig. 3(b) for the fabricated AZO/ZnO/CdS/Mo/SLG heterostructure solar cell, illustrating the different stacked layers. The sputter deposited Mo thin film on the SLG substrate showed columnar growth with thickness  $\sim 1.5 \mu\text{m}$ . The CZTS absorber thin film has been grown on Mo/SLG and cross-sectional SEM micrographs substantiate the nearly uniform well adhered CZTS thin film. The CZTS/Mo interface may consist of an interfacial  $\text{MoS}_2$  layer, grown during the deposition of the CZTS absorber layer and its sulfurization at elevated temperatures. However, no evidence of  $\text{MoS}_2$  is observed in XRD and cross-sectional micrographs within the instrumental resolution. There are reports substantiating the growth of the  $\text{MoS}_2$  layer during the high temperature sulfurization of synthesized CZTS thin film and the observed broadening near the (200) CZTS peak is attributed to the formation of  $\text{MoS}_2$ .<sup>32,33</sup> This thin  $\text{MoS}_2$  layer offers additional benefits for the strong adherence of the CZTS absorber layer over the Mo coated substrate.<sup>32,33</sup> Furthermore, a cross-sectional elemental line mapping is carried out using EDX and results are summarized in Figs. 3(c) and 3(d). The distribution of sulfur across the Mo/CZTS is quite significant in conjunction with molybdenum, substantiating the formation of  $\text{MoS}_2$  near the interface, Fig. 3(c). However it is not easy to distinguish  $\text{MoS}_2$  using EDX measurements, as the characteristic sulfur  $K\alpha$  (2.307 keV) signals overlap nearly at the same energy with molybdenum  $L\alpha$  (2.293 keV). Furthermore, the elemental distributions across the interface are shown in Fig. 3(d), showing the evidence of observed CZTS elemental contribution, as shown in the inset of

Fig. 3(a). The thickness of CZTS absorber thin films for these solar cell structures is  $\sim 2.5 \pm 0.2 \mu\text{m}$  as observed in the cross-sectional micrograph [Fig. 3(b)]. The absorber layer is made of larger and dense grains with some probable voids, causing the poor electrical and photovoltaic response, as discussed later. The thicknesses of wideband gap CdS and ZnO layers are of the order of  $\sim 50 \text{ nm}$  and thus were not visible in the cross-sectional SEM micrographs. The thickness of the top AZO layer has been intentionally kept at  $\sim 1.1 \pm 0.1 \mu\text{m}$  to ensure the high electrical conductivity for efficient photo generated carrier collection.

## B. Optical and electronic characterization

The diffuse reflectance analysis (DRA) measurements are carried out from the 200 nm to 900 nm wavelength range on CZTS/SLG structures and used to calculate the spectral absorptance using the Kubelka-Munk model  $\alpha = \frac{(100-R)^2}{2R}$ , where  $\alpha$  is the absorption coefficient and R is the percent diffuse reflectance.<sup>34</sup> The calculated spectral absorptance ( $\alpha$ ) is used to extrapolate the optical band gap using the Tauc relation  $(\alpha h\nu)^{\frac{1}{n}} = A(h\nu - E_g)$ , where h is Planck's constant,  $\nu$  is incident photon frequency, A is proportionality constant, and  $E_g$  is the band gap of the material. The exponent n can take value 1/2, 3/2, 2, and 3 depending on the nature of optical transition corresponding to direct allowed, direct forbidden, indirect allowed, and indirect forbidden transitions, respectively.<sup>35</sup> The measured  $(\alpha h\nu)^2$  has been plotted against energy  $h\nu$  and is shown in Fig. 3. The linear region with  $(\alpha h\nu)^2 = 0$  intercept suggests the direct optical band gap  $\sim 1.5 \text{ eV}$  for synthesized CZTS thin films.

The controlled non-stoichiometry of the CZTS semiconductor, especially with copper deficiency and excess zinc, has been used to realize the enhanced solar photovoltaic

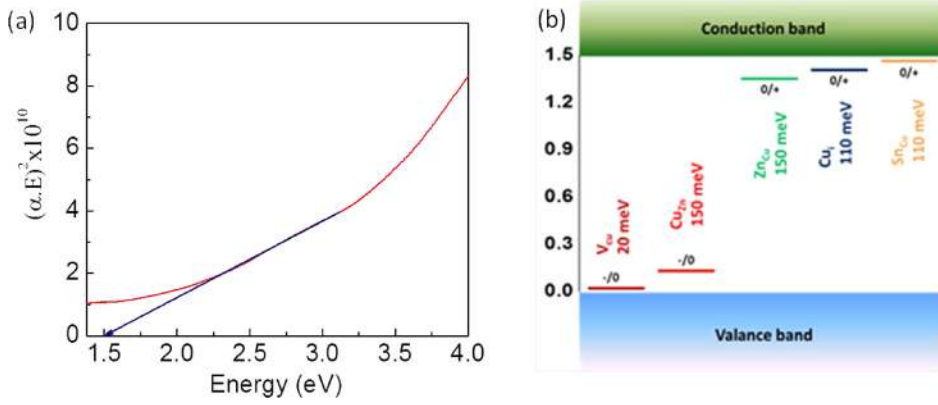


FIG. 4. (a)  $(\alpha E)^2$  versus energy  $E$  (eV) (i.e., Tauc plot with  $n = 1/2$ ) for CZTS/SLG thin films, estimated from the reflectance versus wavelength measurements and (b) schematic representation of possible defect energy levels in CZTS with energy scale on a vertical scale.<sup>36</sup>

response. The important defect states include vacancies at different atomic sites ( $V_{Cu}, V_{Zn}, V_{Sn}$ ) and antisites ( $Cu_{Zn}, Cu_{Sn}, Zn_{Sn}$ ) as acceptor defects, whereas vacancy ( $V_s$ ), interstitial ( $Cu_i, Zn_i$ ), and antisites ( $Zn_{Cu}, Sn_{Zn}, Sn_{Cu}$ ) as donor defects. The relatively lower formation energy of the acceptor defects in CZTS converts it into a p-type semiconductor intrinsically. Near stoichiometric CZTS, the formation energy of defects is very high except  $Cu_{Zn}$  and  $V_{Cu}$  acceptor defects, as schematically represented in Fig. 4(b).<sup>21,37</sup> Thus,  $Cu_{Zn}$  and  $V_{Cu}$  acceptor defects will be contributing effectively in CZTS for the electrical response, whereas other defects will not contribute significantly. The EDX results suggest that the synthesized CZTS films are copper deficient and zinc rich in stoichiometry. This implies that the formation energy for  $V_{Cu}$  and  $Zn_{Sn}$  will decrease significantly, while it will increase for  $Cu_{Zn}$  and  $Sn_{Zn}$  defects thus making  $V_{Cu}$  a dominant acceptor defect level in our CZTS thin films, consistent with the reported literature.<sup>37</sup>

**C. Current–voltage characteristics and open circuit voltage decay**

Current voltage ( $I$ - $V$ ) measurements are carried out on the CZTS absorber based solar cell structures under darkness

and one sun illumination. The measured dark and illuminated  $I$ - $V$  characteristics are summarized in Fig. 5(a) for the solar cell with the highest efficiency among investigated Al:ZnO/ZnO/CdS/CZTS/Mo/SLG heterostructures, with the inset showing the respective device parameters. The series and shunt resistances for the cells are measured using the zero voltage and zero current conditions of  $I$ - $V$  data, respectively. The similar measurements are carried out on such more than five solar cell devices and the photovoltaic efficiency of these cells is  $\sim 1.1\% \pm 0.2\%$ . The current–voltage under dark conditions is shown in Fig. 5(b) and has been fitted using one diode model for the solar cell to extract the photovoltaic device parameters. The measured reverse saturation current density and the ideality factor ( $n$ ), as defined in diode current equation (1), for the photovoltaic device are summarized in the inset of Fig. 5(b).

The one diode DC and AC equivalent circuits are shown in Fig. 5(c) for a solar photovoltaic device.<sup>29</sup> Here,  $R_s$  and  $R_{sh}$  are the series and shunt resistances of the device, with  $I_0$  being reverse saturation resistance. For an AC equivalent circuit, the capacitance ( $C_p$ ) comprises of a parallel combination of diffusion ( $C_d$ ) and transition ( $C_t$ ) diode capacitances and the parallel resistance  $R_p$  is a parallel combination of diodes’ static ( $R_t$ ) and dynamic ( $R_d$ ) resistances. The values

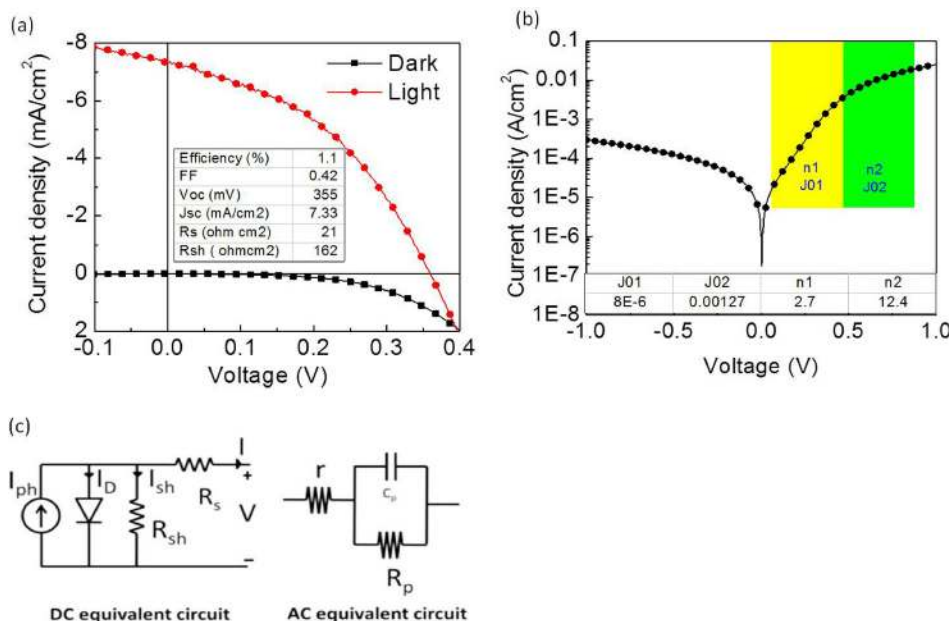


FIG. 5. (a) Current density versus voltage ( $J$ - $V$ ) characteristics under dark and illumination conditions; (b) dark current-voltage characteristics for Al:ZnO/ZnO/CdS/CZTS/Mo/SLG solar cells and (c) DC and AC equivalent circuits of the solar cell, used in simulating the device characteristics.<sup>38</sup>

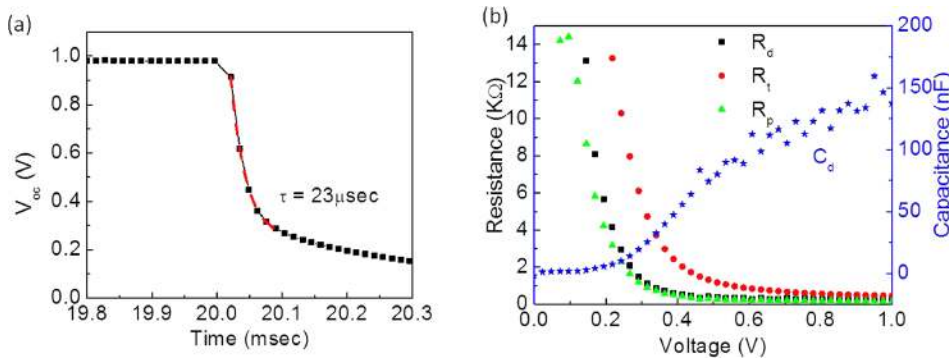


FIG. 6. (a) Open circuit voltage decay (OCVD) plot and (b) variation of resistances and capacitance with applied bias voltage for the Al:ZnO/ZnO/CdS/CZTS/Mo/SLG solar cell.

of these DC and AC device parameters are evaluated using impedance measurements, as discussed later and summarized in Fig. 6(b). The values of  $R_s$  and  $R_{sh}$  are zero and infinite for an ideal diode device and the current voltage relationship can be expressed as

$$I = I_0 \left[ \exp\left(\frac{qV}{nk_B T}\right) - 1 \right], \quad (1)$$

where  $I$  is the diode (device) current,  $I_0$  is the reverse saturation current,  $n$  is an ideality factor,  $q$  is the electronic charge,  $k_B$  is the Boltzmann constant,  $T$  is the temperature in K, and  $V$  is the applied bias voltage across the diode. For large forward bias conditions,  $I/I_0 \gg 1$ , and logarithmic of current can be expressed as

$$\ln(I) = \ln(I_0) + \left(\frac{q}{nK_B T}\right)V. \quad (2)$$

This relation can be used to estimate the reverse saturation current from the intercept  $\ln(I_0)$  and the ideality factor from the slope of the linear portion of  $\ln(I)$  versus  $V$  characteristics at high current region ( $I/I_0 \gg 1$ ) as  $n = \frac{q}{K_B T} \left(\frac{dV}{d\ln(I)}\right)$ . The representative dark current–voltage characteristic is shown in Fig. 5(b) for one of the photovoltaic devices. The different slopes are visible for different forward bias voltage regions. This measurement suggests variation of the ideality factor with applied bias voltage. The reverse saturation current and ideality factor ( $J_{01}$ ,  $n_1$ ) are ( $8 \times 10^{-6}$  A/cm<sup>2</sup>, 2.7) for lower bias voltage  $V < 0.45$  V range. However, the values ( $J_{02}$ ,  $n_2$ ) enhance drastically to ( $1.27 \times 10^{-3}$  A, 12.4) in the higher bias voltage ( $0.45$  V  $< V < 1$  V) window. The relatively large value of the ideality factor suggests that large recombination other than band to band and Shockley-Read-Hall (SRH) is dominating in the lower voltage range and is consistent with the observed large defect density in CZTS thin films. In contrast, the observed very large  $\sim 12.4$  in a higher voltage range is attributed to the accelerated carrier recombination due to the large carrier injection, interfacial defect states, and edge recombination in such heterostructure devices.

#### D. Open circuit voltage decay analysis

Open circuit voltage decay (OCVD) measurements are carried out for the fabricated Al:ZnO/ZnO/CdS/CZTS/Mo/SLG heterostructure photovoltaic devices. A large forward

current is passed across the cell, ensuring the high level of carrier injection, using the fast chrono-potentiometry option in AUTOLAB, followed by open circuit conditions abruptly. The OCVD response of the cell was recorded using PGSTAT302N AUTOLAB, having a bandwidth of 1 MHz, and is shown in Fig. 6(a). Under a high level of injection, minority carrier electron concentration in the p-type CZTS absorber layer is higher than the respective thermal equilibrium value. When forward current is discontinued abruptly and the circuit becomes open, the minority carriers diffuse through the CZTS absorber layer. The minority carrier life time ' $\tau$ ' is related to the open circuit voltage decay rate ( $dV_{oc}/dt$ ) as  $\tau = nk_B T / q \left(\frac{1}{dV_{oc}/dt}\right)$ , where  $n$  is the ideality factor,  $k_B$  is the Boltzmann constant, and  $T$  is temperature in Kelvin.<sup>39</sup> It can be observed that the obtained OCVD curve is nonlinear and decays exponentially. This nonlinear behavior of the OCVD curve can be well explained by the exponential fit of open circuit voltage decay given in the following equation:<sup>40</sup>

$$V_{oc}(t) = \frac{kT}{q} \left[ \exp\left(\frac{qV_0}{k_B T} - 1\right) \right] \exp\left(\frac{-t}{\tau}\right), \quad (3)$$

where  $V_0$  is the open circuit voltage at the termination of excitation. The measured minority carrier life time value obtained from this exponential fit is  $\sim 23 \mu\text{s}$  in these photovoltaic devices. This value is much lower than the earlier reported minority carrier life time by Patel *et al.*<sup>41</sup> for the same system, yet relatively in agreement with that of others' reported work on other systems using the open circuit voltage decay process.<sup>42</sup>

The nonlinear nature of OCVD [Fig. 6(a)], suggests that transition capacitance is dominating over the investigated bias voltage range. The transition capacitance of the photovoltaic device  $C_t = \left(\frac{I}{dV/dt}\right)_{(V=V_b)}$  can be measured by using current  $I$  at bias voltage  $V = V_b$  from dark I-V characteristics [Fig. 5(b)] and voltage decay rate at  $V = V_b$  from OCVD characteristics [Fig. 6(a)]. The current and voltage decay values are  $1.03 \times 10^{-4}$  A and  $4.5 \times 10^3$  V/s, respectively, at  $V_b = 0.35$  V, leading to 22.8 nF transition capacitance for the photovoltaic device. The static ( $R_{\text{static}} = (V/I)_{V_b}$ ) and dynamic ( $R_{\text{dynamic}} = (1/(dI/dV))_{V_b}$ ) resistances are 3.39 k $\Omega$  and 0.8 k $\Omega$ , respectively, at  $V_b = 0.35$  V. Thus, the effective parallel resistance ( $R_p = R_{\text{static}} || R_{\text{dynamic}}$ ) for the photovoltaic device is  $\sim 0.64$  k $\Omega$ . The measured diffusion capacitance

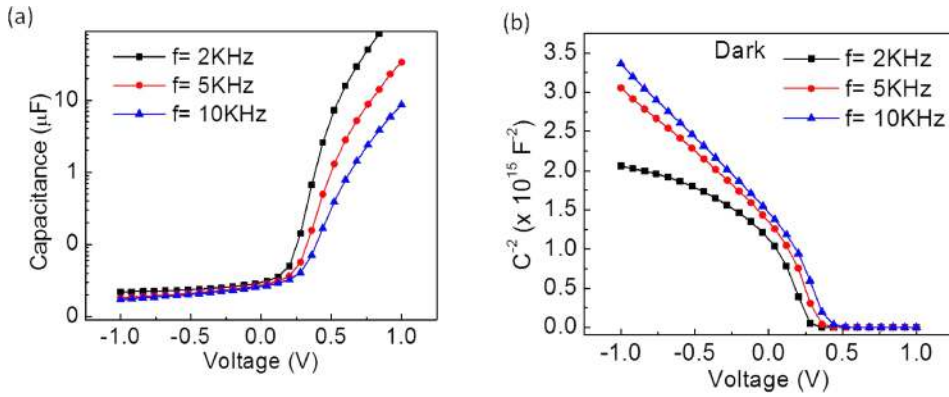


FIG. 7. Capacitance–voltage characteristics (a) and Mott-Schottky plots (b) for the Al:ZnO/ZnO/CdS/CZTS/Mo/SLG solar cell, measured at different frequencies.

$C_{diffusion} = \frac{\tau}{R_p}$  is 35.5 nF at  $V_b = 0.35$  V. The variation of cell resistances and diffusion capacitance against the bias voltage are summarized in Fig. 6(b).

### E. Capacitance-voltage (C-V) analysis

The capacitance-voltage measurements are carried out at different frequencies under applied DC bias voltages and are shown in Fig. 7(a).

The total capacitance of the device is originating from the depletion and chemical capacitances, where depletion capacitance (or space charge capacitance) is due to the depletion region under reverse bias conditions. This is analogous to the parallel plate capacitor with capacitance  $C_{dl} = \frac{\epsilon_0 \epsilon_r A}{W}$ , where  $\epsilon_0$  is the permittivity of free space,  $\epsilon_r$  is the permittivity of the material,  $A$  is the area of the solar cell, and  $W$  is the depletion width at the interface, given as  $W = \left( \frac{2\epsilon_0 \epsilon_r V_{bi}}{qN} \right)^{1/2}$ ; with  $N = \frac{N_A N_D}{N_A + N_D}$ , where  $N_A$  and  $N_D$  are the doping concentration of the p and n region, respectively, and  $V_{bi}$  is the built in potential across the junction.<sup>43</sup> The chemical capacitance per unit area is given as  $C_\mu = \frac{q^2 L n_0}{k_B T} e^{\frac{qV}{k_B T}}$ , where  $L$  is the thickness of the charge accumulation layer,  $n_0$  is the minority carrier concentration at equilibrium,  $\eta$  is the diode ideality factor,  $k_B$  is the Boltzmann constant, and  $T$  is temperature in Kelvin.<sup>44</sup> The exponential dependence of chemical capacitance dominates in the total capacitance of the solar cell at sufficiently high forward bias as shown in Fig. 7(a), similar to that of the silicon solar cell.<sup>44</sup> The capacitance decreases at a fixed polarization potential with increasing frequency and increases exponentially with increasing polarization potential at a fixed frequency, as can be seen in Fig. 7(a). This is because of insensitiveness of absorber traps at high frequencies and thus, effectively traps do not contribute, reducing the effective charge, resulting in lower device capacitance ( $C = Q/V$ ).

The capacitance–voltage data are used to derive the Mott-Schottky (MS) plots (inverse of squared capacitance versus applied voltage) at different measured frequencies and are summarized in Fig. 7(b). The choice of frequency for the Mott schottky analysis is a critical parameter. The parasitic resistance of a diode due to the bulk material ( $R_s$ ) is usually small and to ensure that it is not affecting the measurements, the selected frequency for measurements should be relatively small following the condition  $R_s \ll 1/\omega C$ , where  $\omega$  is the angular

frequency and  $C$  is the junction capacitance.<sup>45</sup> All the measurements are carried out under this constraint, ensuring that the reactive part is much greater than that of the resistive part of the diode impedance. Relatively high frequencies are considered for these MS measurements to avoid the low frequency dispersion in such measurements. These MS plots show a significant change in the slope near zero bias while crossing the applied bias voltage from the negative to positive potential. The change has been attributed to enhanced carrier density with positive potential bias conditions [Fig. 7(b)]. In addition, the slope of the linear portion of these MS curve is nearly identical for all measured frequencies, whereas the point of intersection of this linear region at  $1/C^2 = 0$  differs for these measured frequencies. The possible reason for the marginal deviation may be appearing due to the localized deep states in the absorber material. At higher frequency, the contribution from the deep states is not significant and the major contribution in the capacitance mainly originates from the modulation of majority carriers near the edge of the depletion region. In addition to the presence of a back contact barrier, the device capacitances strongly depend on the measuring frequency<sup>46</sup> and this gives rise to the shift in the point of intersection of the linear portion of Mott schottky plots, as can be seen in Fig. 7(b). This is related to the variation of the depletion width of the back contact junction at different frequencies.

Considering the abrupt hetero-junction, the acceptor defect concentration ( $N_a$ ) in the p-type CZTS absorber, and flat band potential ( $V_{fb}$ ) are determined using the following expression:<sup>47</sup>

$$\frac{A^2}{C^2} = \left[ \frac{2}{q\epsilon_0\epsilon_{CdS}\epsilon_{CZTS}} \right] \left[ \frac{N_d\epsilon_{CdS} + N_a\epsilon_{CZTS}}{N_a N_d} \right] (V_{fb} - V), \quad (4)$$

where  $A$  is the area of the junction,  $q$  is electronic charge,  $\epsilon_0$  is permittivity of vacuum,  $\epsilon_{CdS}$  is relative permittivity of CdS,  $\epsilon_{CZTS}$  is relative permittivity of CZTS, and  $N_d$  is total n-region ionized donor defect concentration. This expression for a  $n^+ - p$  hetero-junction simplifies into

$$\frac{A^2}{C^2} = \left[ \frac{2}{q\epsilon_0\epsilon_{CZTS}N_d} \right] (V_{fb} - V). \quad (5)$$

This has been used to estimate the effective acceptor concentration for CZTS absorber materials. The depletion width  $W_{dep} = \frac{\epsilon_0\epsilon_{CZTS}}{C_{dep}}$  is  $\sim 20.5$  nm for the investigated heterostructures with the relative dielectric constant of CZTS  $\sim 6.95$ ,

measured acceptor concentration  $\sim 5.8 \times 10^{17} \text{ cm}^{-3}$  in conjunction with  $\sim 0.35 \text{ V}$  flat band potential. The built in potential ( $V_{bi} = V_{fb} - k_B T/q$ ) is  $\sim 0.32 \text{ V}$  for the investigated solar cell structures. The high acceptor concentration in the device has been attributed to the observed lower photovoltaic efficiency of the investigated structure. The one dimensional (1D) device simulation has been carried out using the measured carrier concentration, defect levels, and other physical parameters, and calculated results substantiate the observed lower efficiency consistent with the other available reports.<sup>48</sup>

**F. Impedance spectroscopy analysis**

The impedance spectroscopic measurements are carried out for these fabricated solar cells. The Nyquist plots and the complex plane representation of the impedance data at zero bias are shown in Fig. 8 for the Al:ZnO/ZnO/CdS/CZTS/Mo/SLG heterostructure photovoltaic device. The respective equivalent circuit is shown as an inset in these plots, which

are used for extracting the probable resistive and capacitive components for these photovoltaic devices.<sup>49</sup> The respective percent errors between measured and simulated impedances are shown in the respective right panel of Fig. 8. The semi-circular nature of these Nyquist plots substantiates the dominance of the space charge region in these photovoltaic cells.

The simplest circuit is characterized by the series resistance ( $R_s$ ) and a resistance-capacitance loop ( $R_j$ - $C_j$ ), describing the CdS/CZTS hetero-junction. This is named M1 hereafter. The series resistance ( $R_s$ ) includes all the contact and material resistances such as resistance of the connecting lid, wire, Mo back contact, and Al:ZnO/ZnO front window layer. The simulated equivalent circuit data show a large deviation in the intermediate frequency range, as can be seen from the error plots [right panel, Fig. 8(a)]. This deviation may be attributed to the non-ohmic back contacts between CZTS and Mo layers. To account for these contributions, an additional resistance-capacitance loop ( $R_b$ - $C_b$ ) has been added in the equivalent circuit in series with the  $R_j$ - $C_j$  loop,

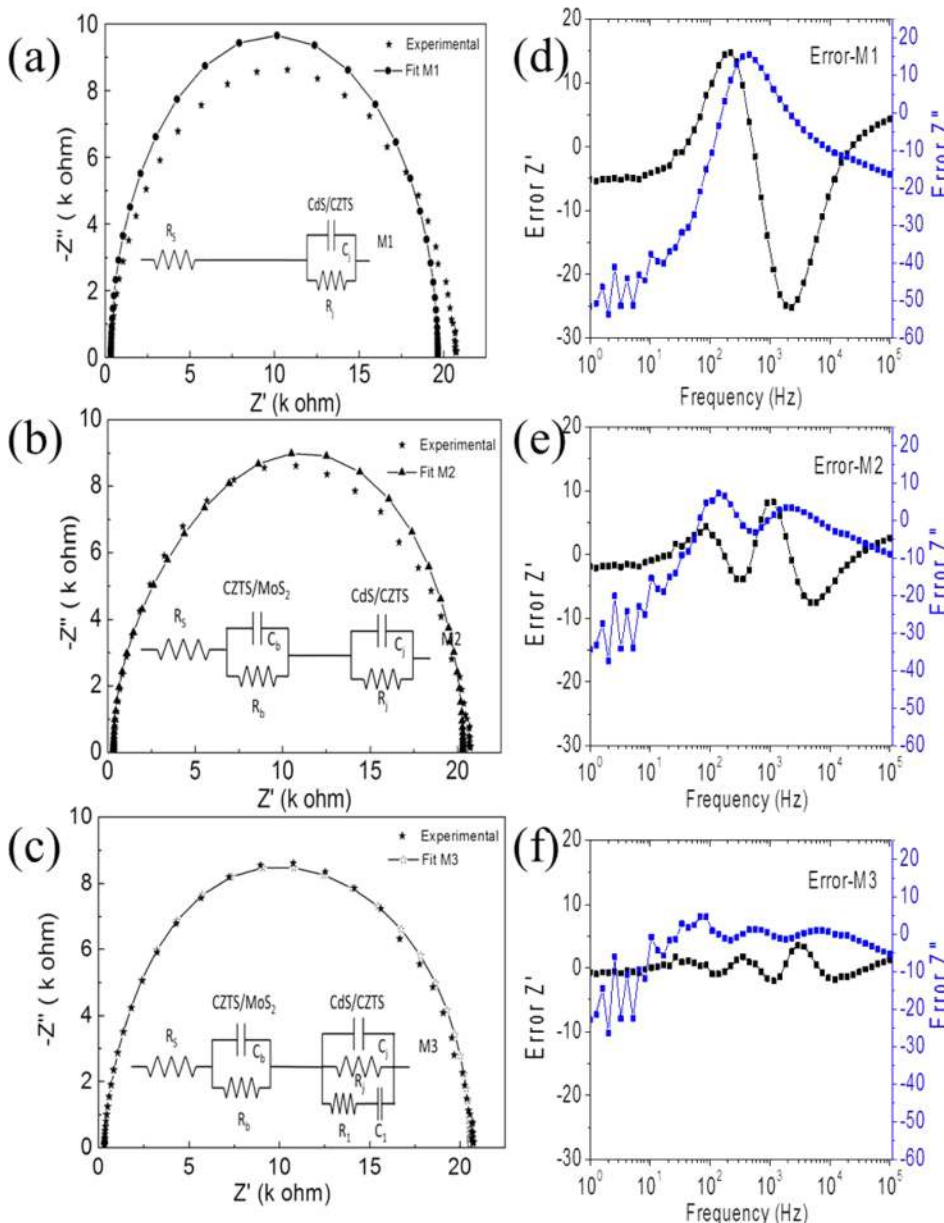


FIG. 8. (a) Impedance spectrograph for the Al:ZnO/ZnO/CdS/CZTS/Mo/SLG solar cell with three different equivalent circuit models M1, M2, and M3, as explained in [(a)–(c)] and corresponding error in [(d)–(f)]. where M3 corresponds to the best fit to the measured experimental impedance spectrograph.

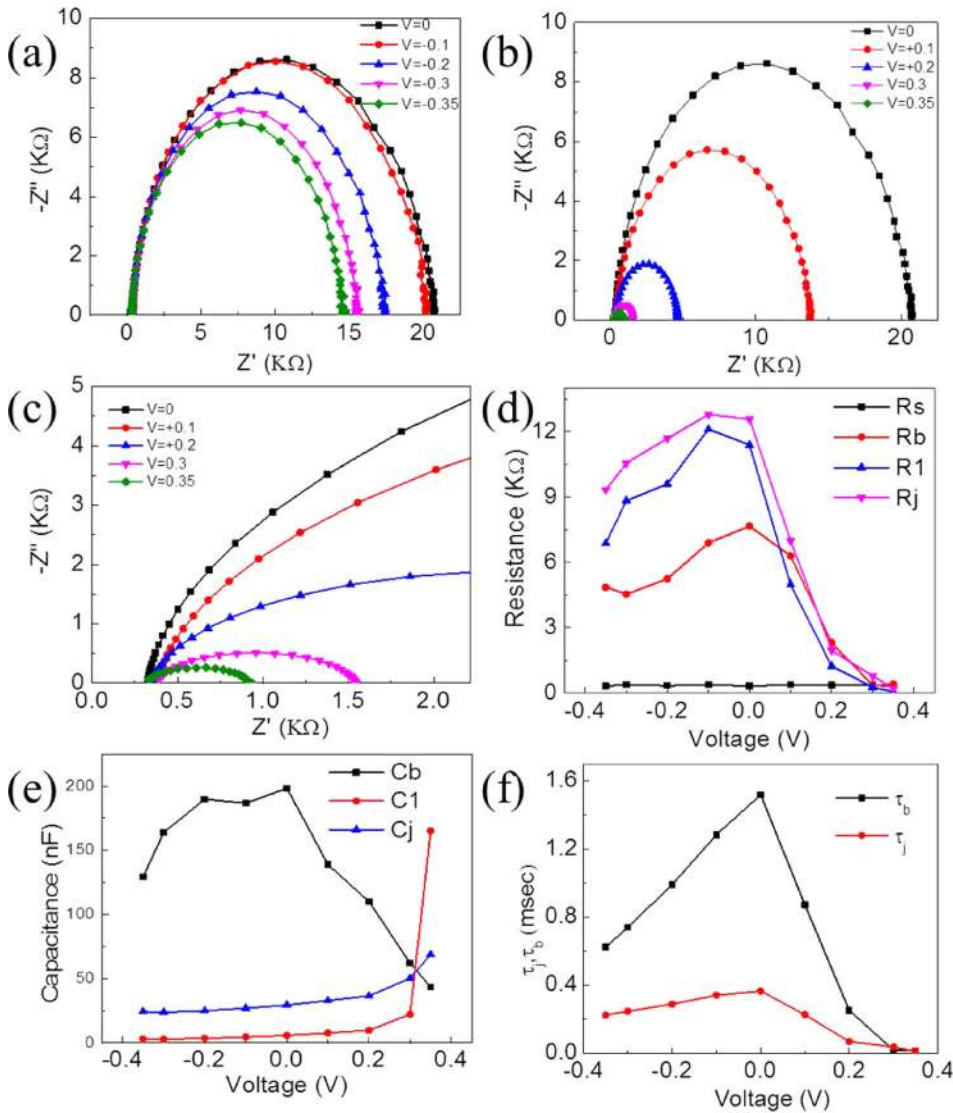


FIG. 9. Complex plane impedance plot in the dark under (a) forward bias and (b) reverse bias; (c) zoom view of the forward biased impedance plot, (d) resistance variation, (e) capacitance variation, and (f) minority carrier lifetimes ( $\tau_j = R_j C_j$  and  $\tau_b = R_b C_b$ ) as a function of bias voltage for Al:ZnO/CdS/CZTS/Mo/SLG solar cells.

as shown in the inset in Fig. 8(b) and named M2 hereafter. Thus, including the contribution of such non-ohmic contacts is important to account for the formation of a thin MoS<sub>2</sub> layer during CZTS growth (as substantiated from the capacitance-voltage measurement). This has also improved the simulated impedances, as respective impedance errors are relatively lower than that of the M1 equivalent circuit.

However, there are still substantial differences between experimental and simulated equivalent (M2 circuit) impedance data. This suggests that the contribution of junction inhomogeneity in conjunction with different defect states in the CdS/CZTS heterojunction is important and cannot be ignored. Considering the same, a series resistance-capacitance (R1-C1) pair has been included in parallel with the Rj-Cj CdS/CZTS heterojunction loop, as shown in the inset in Fig. 8(c). This equivalent circuit is named M3 hereafter. The R1-C1 pair represents the contribution of the spatial inhomogeneity and trap states, originating from the absorber grain boundaries, near the CdS/CZTS heterojunction. The experimental data fit the best with simulated M3 equivalent circuit data, as shown in Fig. 8(c) and the respective impedance error plot. The maximum error in the fitting of  $Z'$  improves with including the trap states in the M3

equivalent circuit ( $\sim 2\%$ ) with respect to that of M2 ( $\sim 8\%$ ) and M1 ( $\sim 25\%$ ) equivalent circuits. The observed deviation in the low frequency region is attributed to the improper contact between Al:ZnO and contact lid, whereas the deviations in high frequency regions are attributed to the inhomogeneous absorber layer and low quality hetero-interface.

The impedance measurements are also carried out at different bias voltages with semicircular impedance characteristics, as shown in Fig. 9(a) under reverse bias conditions and in Fig. 9(b) under forward bias conditions. The equivalent circuit M3 comprising of three sections, first one consisting of  $R_s$  is equivalent to the series resistance of the device, second one comprising parallel combination of ( $R_b-C_b$ ) equivalent to the back contact junction, and the third one with parallel combination of ( $R_j-C_j$ ) in parallel with series ( $R_1-C_1$ ) combination, equivalent to the heterojunction behavior of the CdS/CZTS interface, has been used to simulate these impedance measurements. The extracted circuit parameters at different bias voltages are summarized in Figs. 9(e) and 9(f). The semicircle nature of these Nyquist plots shrinks with increasing the magnitude of bias voltage under both reverse and forward condition, which is more pronounced in the case of forward bias voltages and higher forward bias voltage

regions are shown in Fig. 9(c) for clarity. This is consistent with the enhancement of carriers under forward bias, increasing the conductivity and thus reducing the impedances.

The measured impedance data were fitted with circuit M3 and the measured series resistance is nearly constant ( $355 \pm 20 \Omega$ ) for these Al:ZnO/ZnO/CdS/CZTS/Mo/SLG photovoltaic devices. This observed high value of series resistance is attributed to the Schottky junction formed at the back contact between Mo and CZTS interface due to the formation of the MoS<sub>2</sub> layer. The back contact junction is reverse biased under forward bias conditions and thus, the current conduction is limited to the reverse saturation current, causing the enhanced series resistance of the cell.<sup>10</sup> The back contact junction starts limiting the current and decreasing the back contact junction capacitance and thus, the overall capacitance of the photovoltaic device with increasing the forward bias voltage.<sup>50</sup> The lower open circuit voltage for the cell is also associated with the generated negative photovoltage at the back contact junction.<sup>50</sup> The back contact capacitance ( $C_b$ ) shows a decreasing trend with increasing reverse and forward bias voltages.

The nature of impedance measurements is consistent with the change in diameter of the semicircle with the bias potential. The hetero-junction capacitance ( $C_j$ ) behaves as the p-n junction under applied potential. The slight increase in junction capacitance with decreasing reverse bias can be understood in terms of depletion region capacitance. This decrease in capacitance is mainly attributed to the decrease in the space charge region width ( $W$ ) with decreasing reverse bias. When the hetero junction enters into the forward bias region, an exponential increase in capacitance has been observed. This dependence of  $C_j$  is attributed to the inclusion of diffusion capacitance because of increased diffusion current. The shunt resistances  $R_j$  and  $R_b$  represent the leakage path, originating due to the generation and recombination in the depletion regions. The measured characteristic time constants for the CdS/CZTS heterojunction ( $\tau_j$ ) and back contact junction between CZTS and MoS<sub>2</sub>/Mo interface ( $\tau_b$ ) are plotted in Fig. 9(f). The two time constants differ significantly from one another, as they represent charging/discharging behavior in different sections of the device. Similar observations were reported for CdTe/CdS solar cells.<sup>15,16</sup> The values of the time constant obtained from the impedance data fitting at  $V = 0.35 \text{ V}$  are  $\tau_j = 13.3 \mu\text{s}$  and  $\tau_b = 17.8 \mu\text{s}$ . The resultant time constant  $\tau = (\tau_j \tau_b / \tau_j + \tau_b)$  is  $\sim 7.6 \mu\text{s}$  for the investigated photovoltaic devices. The time constant obtained from the impedance measurement is relatively smaller than that obtained from the OCVD analysis. The time constants measured under light and dark conditions should give similar values of minority carrier life time.<sup>51,52</sup> However, slight variation in the obtained time constant value from the two methods is possibly due to the high population of injected charge carrier during OCVD measurements and the non linear characteristics of the OCVD curve that makes it difficult to determine the accurate slope for time constant measurement.

#### IV. CONCLUSION

Al:ZnO/ZnO/CdS/CZTS/Mo/SLG heterostructure solar photovoltaic devices are fabricated using the solution

derived spin coated optimized CZTS absorber layer. The electrical measurements suggest the contribution of high series and relatively low shunt resistances which may be responsible for the observed photovoltaic response for these device structures. The impedance data are simulated with an equivalent circuit and the best fit to the experimental data suggests that there is significant contribution from back contact between CZTS and Mo and trap states near the CdS/CZTS interface. The minority carrier life time is  $\sim 23 \mu\text{s}$ , as observed from open circuit voltage decay measurements. This is a bit larger with respect to the minority carrier life time  $\sim 8 \mu\text{s}$ , observed from impedance measurements. The observed difference in the minority carrier life time is possibly due to the nonlinear characteristics of the voltage decay curve, which leads to difficulties in determining the accurate slope and thus may lead to different values. These studies provide the detailed electrical studies on sol-gel derived photovoltaic devices, inferring the relative device parameters, causing the observed poor efficiencies.

#### ACKNOWLEDGMENTS

The authors acknowledge the Department of Science and Technology (DST), Government of India, through Grant Nos. DST/INT/Mexico/P-02/2016 and DST/INR/ISR/P-12/2014 for carrying out the experimental work.

- <sup>1</sup>M. C. Wei, S. J. Chang, C. M. Lee, and R. W. Chuang, "The challenge of commercialized crystalline silicon solar cell," *2nd Electronics System-Integration Technology Conference, 2008, ESTC 2008* (IEEE, 2008).
- <sup>2</sup>P. Jackson, D. Hariskos, R. Wuerz, O. Kiowski, A. Bauer, T. M. Friedlmeier, and M. Powalla, "Properties of Cu(In,Ga)Se<sub>2</sub> solar cells with new record efficiencies up to 21.7%," *Phys. Status Solidi -Rapid Res. Lett.* **9**, 28–31 (2015).
- <sup>3</sup>R. M. Geishardt, M. Topic, and J. R. Sites, "Status and potential of CdTe solar-cell efficiency," *IEEE J. Photovoltaics* **5**, 1217–1221 (2015).
- <sup>4</sup>A. Hagfeldt, G. Boschloo, L. Sun, L. Kloo, and H. Pettersson, "Dye-Sensitized Solar Cells," *Chem. Rev.* **110**, 6595–6663 (2010).
- <sup>5</sup>L. Lu, T. Zheng, Q. Wu, A. M. Schneider, D. Zhao, and L. Yu, "Recent advances in bulk heterojunction polymer solar cells," *Chem. Rev.* **115**, 12666–12731 (2015).
- <sup>6</sup>G. Li, R. Zhu, and Y. Yang, "Polymer solar cells," *Nat. Photonics* **6**, 153–161 (2012).
- <sup>7</sup>W. Wang, M. T. Winkler, O. Gunawan, T. Gokmen, T. K. Todorov, Y. Zhu, and D. B. Mitzi, "Device characteristics of CZTSSe thin-film solar cells with 12.6% efficiency," *Adv. Energy Mater.* **4**, 1–5 (2014).
- <sup>8</sup>K.-J. Yang, D.-H. Son, S.-J. Sung, J.-H. Sim, Y.-I. Kim, S.-N. Park, D.-H. Jeon, J. Kim, D.-K. Hwang, C.-W. Jeon, D. Nam, H. Cheong, J.-K. Kang, and D.-H. Kim, "A band-gap-graded CZTSSe solar cell with 12.3% efficiency," *J. Mater. Chem. A* **4**, 10151–10158 (2016).
- <sup>9</sup>J. Kim, H. Hiroi, T. K. Todorov, O. Gunawan, M. Kuwahara, T. Gokmen, D. Nair, M. Hopstaken, B. Shin, Y. S. Lee, W. Wang, H. Sugimoto, and D. B. Mitzi, "High efficiency Cu<sub>2</sub>ZnSn(S,Se)<sub>4</sub> solar cells by applying a double in 2S3/CdS Emitter," *Adv. Mater.* **26**, 7427–7431 (2014).
- <sup>10</sup>O. Gunawan, T. K. Todorov, and D. B. Mitzi, "Loss mechanisms in hydrazine-processed Cu<sub>2</sub>ZnSn(Se,S)<sub>4</sub> solar cells," *Appl. Phys. Lett.* **97**, 233506 (2010).
- <sup>11</sup>K. Wang, O. Gunawan, T. Todorov, B. Shin, S. J. Chey, N. A. Bojarczuk, D. Mitzi, and S. Guha, "Thermally evaporated Cu<sub>2</sub>ZnSnS<sub>4</sub> solar cells," *Appl. Phys. Lett.* **97**, 143508 (2010).
- <sup>12</sup>L. Yin, G. Cheng, Y. Feng, Z. Li, C. Yang, and X. Xiao, "Limitation factors for the performance of kesterite Cu<sub>2</sub>ZnSnS<sub>4</sub> thin film solar cells studied by defect characterization," *RSC Adv.* **5**, 40369–40374 (2015).
- <sup>13</sup>I. Repins, C. Beall, N. Vora, C. Dehart, D. Kuciauskas, P. Dippo, B. To, J. Mann, W. Hsu, A. Goodrich, and R. Noufi, *Sol. Energy Mater. Sol. Cells* **101**, 154–159 (2012).

- <sup>14</sup>Y. T. Hsieh, Q. Han, C. Jiang, T. Bin Song, H. Chen, L. Meng, H. Zhou, and Y. Yang, "Efficiency enhancement of Cu<sub>2</sub>ZnSn(S,Se)<sub>4</sub> solar cells via alkali metals doping," *Adv. Energy Mater.* **6**, 1–6 (2016).
- <sup>15</sup>Z. Su, K. Sun, Z. Han, H. Cui, F. Liu, Y. Lai, J. Li, X. Hao, Y. Liu, and M. A. Green, "Fabrication of Cu<sub>2</sub>ZnSnS<sub>4</sub> solar cells with 5.1% efficiency via thermal decomposition and reaction using a non-toxic sol-gel route," *J. Mater. Chem. A* **2**, 500–509 (2014).
- <sup>16</sup>H. Katagiri, N. Sasaguchi, S. Hando, S. Hoshino, J. Ohashi, and T. Yokota, "Preparation and evaluation of Cu<sub>2</sub>ZnSnS<sub>4</sub> thin films by sulfurization of E-B evaporated precursors," *Sol. Energy Mater. Sol. Cells* **49**, 407–414 (1997).
- <sup>17</sup>K. Tanaka, M. Oonuki, N. Moritake, and H. Uchiki, "Cu<sub>2</sub>ZnSnS<sub>4</sub>/Cu<sub>2</sub>ZnSnS<sub>4</sub> thin film solar cells prepared by non-vacuum processing," *Sol. Energy Mater. Sol. Cells* **93**, 583–587 (2009).
- <sup>18</sup>N. Moritake, Y. Fukui, M. Oonuki, K. Tanaka, and H. Uchiki, "Preparation of Cu<sub>2</sub>ZnSnS<sub>4</sub> thin film solar cells under non-vacuum condition," *Phys. Status Solidi Curr. Top. Solid State Phys.* **6**, 1233–1236 (2009).
- <sup>19</sup>K. Tanaka, Y. Fukui, N. Moritake, and H. Uchiki, "Chemical composition dependence of morphological and optical properties of Cu<sub>2</sub>ZnSnS<sub>4</sub> thin films deposited by sol-gel sulfurization and Cu<sub>2</sub>ZnSnS<sub>4</sub> thin film solar cell efficiency," *Sol. Energy Mater. Sol. Cells* **95**, 838–842 (2011).
- <sup>20</sup>M. Courel, E. Valencia-Resendiz, F. A. Pulgarín-Agudelo, and O. Vigil-Galán, "Determination of minority carrier diffusion length of sprayed-Cu<sub>2</sub>ZnSnS<sub>4</sub> thin films," *Solid State Electron.* **118**, 1–3 (2016).
- <sup>21</sup>M. Courel, E. Valencia-Resendiz, J. A. Andrade-Arvizu, E. Saucedo, and O. Vigil-Galán, "Towards understanding poor performances in spray-deposited Cu<sub>2</sub>ZnSnS<sub>4</sub> thin film solar cells," *Sol. Energy Mater. Sol. Cells* **159**, 151–158 (2017).
- <sup>22</sup>X. Jin, J. Li, G. Chen, C. Xue, W. Liu, and C. Zhu, "Preparation of Cu<sub>2</sub>ZnSnS<sub>4</sub>-based thin film solar cells by a combustion method," *Sol. Energy Mater. Sol. Cells* **146**, 16–24 (2016).
- <sup>23</sup>O. Vigil-Galán, M. Courel, M. Espindola-Rodriguez, D. Jiménez-Olarte, M. Aguilar-Frutis, and E. Saucedo, "Electrical properties of sprayed Cu<sub>2</sub>ZnSnS<sub>4</sub> thin films and its relation with secondary phase formation and solar cell performance," *Sol. Energy Mater. Sol. Cells* **132**, 557–562 (2015).
- <sup>24</sup>E. M. Mkawi, K. Ibrahim, M. K. M. Ali, M. A. Farrukh, and A. S. Mohamed, "Influence of triangle wave pulse on the properties of Cu<sub>2</sub>ZnSnS<sub>4</sub> thin films prepared by single step electrodeposition," *Sol. Energy Mater. Sol. Cells* **130**, 91–98 (2014).
- <sup>25</sup>M. Kumar, A. Dubey, N. Adhikari, S. Venkatesan, and Q. Qiao, "Strategic review of secondary phases, defects and defect-complexes in kesterite CZTS-Se solar cells," *Energy Environ. Sci.* **8**, 3134–3159 (2015).
- <sup>26</sup>G. K. Gupta and A. Dixit, "Effect of precursor and composition on the physical properties of the low-cost solution processed Cu<sub>2</sub>ZnSnS<sub>4</sub> thin film for solar photovoltaic application," *J. Renewable Sustainable Energy* **9**, 13502 (2017).
- <sup>27</sup>T. J. Huang, X. Yin, G. Qi, and H. Gong, "CZTS-based materials and interfaces and their effects on the performance of thin film solar cells," *Phys. Status Solidi-Rapid Res. Lett.* **8**, 735–762 (2014).
- <sup>28</sup>M. Cohen, "X-ray diffraction Addison-Wesley metallurgy series," *J. Chem. Inf. Modell.* **53**, 1689–1699 (1956).
- <sup>29</sup>G. K. Williamson and R. E. Smallman, "III. Dislocation densities in some annealed and cold-worked metals from measurements on the X-ray debye-scherrer spectrum," *Philos. Mag.* **1**, 34–46 (1956).
- <sup>30</sup>P. Bindu and S. Thomas, "Estimation of lattice strain in ZnO nanoparticles: X-ray peak profile analysis," *J. Theor. Appl. Phys.* **8**, 123–134 (2014).
- <sup>31</sup>B. P. Rand, J. Genoe, P. Heremans, and J. Poortmans, "Solar cells utilizing small molecular weight organic semiconductors," *Prog. Photovoltaics Res. Appl.* **15**, 659–676 (2007).
- <sup>32</sup>B. Shin, N. A. Bojarczuk, and S. Guha, "On the kinetics of MoSe<sub>2</sub> interfacial layer formation in chalcogen-based thin film solar cells with a molybdenum back contact," *Appl. Phys. Lett.* **102**, 091907 (2013).
- <sup>33</sup>H. Cui, X. Liu, F. Liu, X. Hao, N. Song, C. Yan, H. Cui, X. Liu, F. Liu, X. Hao, N. Song, and C. Yan, "Boosting Cu<sub>2</sub>ZnSnS<sub>4</sub> solar cells efficiency by a thin Ag intermediate layer between absorber and back contact," *Appl. Phys. Lett.* **104**, 041115 (2014).
- <sup>34</sup>V. Džimbeg-malčić, Ž. Barbarić-mikočević, and K. Itrić, "Kubelka-Munk theory in describing optical properties of paper (I)," *Tech. Gazette* **1**, 117–124 (2011).
- <sup>35</sup>B. D. Viezbicke, S. Patel, B. E. Davis, and D. P. Birnie, "Evaluation of the Tauc method for optical absorption edge determination: ZnO thin films as a model system," *Phys. Status Solidi* **11**, 1700–1710 (2015).
- <sup>36</sup>X. Lin, A. Ennaoui, S. Levchenko, T. Dittrich, J. Kavalakkatt, S. Kretschmar, T. Unold, and M. C. Lux-Steiner, "Defect study of Cu<sub>2</sub>ZnSn(SxSe1-x)<sub>4</sub> thin film absorbers using photoluminescence and modulated surface photovoltage spectroscopy," *Appl. Phys. Lett.* **106**, 013903 (2015).
- <sup>37</sup>S. Chen, A. Walsh, X.-G. Gong, and S.-H. Wei, "Classification of lattice defects in the kesterite Cu(2) ZnSnS(4) and Cu(2) ZnSnSe(4) earth-abundant solar cell absorbers," *Adv. Mater.* **25**(11), 1522–1539 (2013).
- <sup>38</sup>C. Zhang, J. Zhang, Y. Hao, Z. Lin, and C. Zhu, "A simple and efficient solar cell parameter extraction method from a single current-voltage curve," *J. Appl. Phys.* **110**, 064504 (2011).
- <sup>39</sup>D. K. Schroder, *Semiconductor Material and Device Characterization*, 3rd ed. (John Wiley and Sons, Inc., 2005).
- <sup>40</sup>J. E. Mahan, T. W. Ekstedt, R. I. Frank, and R. Kaplow, "Measurement of minority carrier lifetime in solar cells from photo-induced open-circuit voltage decay," *IEEE Trans. Electron Devices* **26**, 733–739 (1979).
- <sup>41</sup>M. Patel, I. Mukhopadhyay, and A. Ray, "Study of the junction and carrier lifetime properties of a spray-deposited CZTS thin-film solar cell," *Semicond. Sci. Technol.* **28**, 55001 (2013).
- <sup>42</sup>M. Tapajna, J. Pjenčak, A. Vrbický, P. Kudela, and L. Harmatha, "Application of open circuit voltage decay to the characterization of epitaxial layer," *J. Electr. Eng.* **55**(9), 239–244 (2004).
- <sup>43</sup>S. M. Sze and K. K. Ng, *Physics of Semiconductor Devices* (Wiley-Interscience, 2007).
- <sup>44</sup>I. Mora-Sero, G. Garcia-Belmonte, P. P. Boix, and A. V. Miguel, "Impedance spectroscopy characterisation of highly efficient silicon solar cells under different light illumination intensities," *Energy Environ. Sci.* **6**, 678–686 (2009).
- <sup>45</sup>A. Zekry, M. Abdel-Naby, H. F. Ragaie, and F. E. El Akkad, "Capacitance and conductance of ZnxCd1-xS/ZnTe heterojunctions," *IEEE Trans. Electron Devices* **40**, 259–266 (1993).
- <sup>46</sup>J. Ge, J. Chu, Y. Yan, J. Jiang, and P. Yang, "Co-electroplated kesterite bifacial thin-film solar cells: A study of sulfurization temperature," *ACS Appl. Mater. Interfaces* **7**, 10414–10428 (2015).
- <sup>47</sup>P. A. Fernandes, P. M. P. Salomé, A. F. Sartori, J. Malaquias, A. F. Da Cunha, B.-A. Schubert, J. C. González, and G. M. Ribeiro, "Effects of sulfurization time on Cu<sub>2</sub>ZnSnS<sub>4</sub> absorbers and thin films solar cells obtained from metallic precursors," *Sol. Energy Mater. Sol. Cells* **115**, 157–165 (2013).
- <sup>48</sup>S. R. Meher, L. Balakrishnan, and Z. C. Alex, "Analysis of Cu<sub>2</sub>ZnSnS<sub>4</sub>/CdS based photovoltaic cell: A numerical simulation approach," *Superlattices Microstruct.* **100**, 703–722 (2016).
- <sup>49</sup>P. A. Fernandes, A. F. Sartori, P. M. P. Salomé, J. Malaquias, A. F. da Cunha, M. P. F. Grac, a, and J. C. González, "Admittance spectroscopy of Cu<sub>2</sub>ZnSnS<sub>4</sub> based thin film solar cells," *Appl. Phys. Lett.* **100**, 233504 (2012).
- <sup>50</sup>J. Ge, J. Chu, J. Jiang, Y. Yan, and P. Yang, "Characteristics of substituted CZTS thin film and bifacial solar cell," *ACS Appl. Mater. Interfaces* **6**, 21118–21130 (2014).
- <sup>51</sup>Y. Y. Proskuryakov, K. Durose, M. K. Al Turkestani, I. Mora-Seró, G. Garcia-Belmonte, F. Fabregat-Santiago, J. Bisquert, V. Barrioz, D. Lamb, S. J. C. Irvine, and E. W. Jones, "Impedance spectroscopy of thin-film CdTe/CdS solar cells under varied illumination," *J. Appl. Phys.* **106**, 044507 (2009).
- <sup>52</sup>M. Patel and A. Ray, "Evaluation of back contact in spray deposited SnS thin film solar cells by impedance analysis," *ACS Appl. Mater. Interfaces* **6**, 10099–10106 (2014).